Revised version resubmitted to *Physical Review Materials* on 06/05/2017

Potential Resolution to the "Doping Puzzle" in Iron Pyrite: Carrier Type Determination by Hall Effect and Thermopower

Xin Zhang[1], Mengqun Li[2], Jeff Walter[1], Liam O'Brien[1,3], Michael A. Manno[1], Bryan Voigt[1], Frazier Mork[1], Sergey V. Baryshev[4,5], James Kakalios[2], Eray S. Aydil*[1] and Chris Leighton*[1]

[1]*Department of Chemical Engineering and Materials Science, University of Minnesota, Minneapolis, MN 55455, USA*

[2]*School of Physics and Astronomy, University of Minnesota, Minneapolis, MN 55455, USA*

[3]*Department of Physics, University of Liverpool, Liverpool, L69 7ZE, UK*

[4]*Materials Science Division, Argonne National Laboratory, Argonne, IL 60439, USA*

[5]*Euclid TechLabs, Bolingbrook, IL 60440, USA*

Pyrite FeS_2 has outstanding potential as an earth-abundant, low-cost, non-toxic photovoltaic, but underperforms dramatically in solar cells. While the full reasons for this are not clear, one certain factor is the inability to understand and control doping in FeS_2. This is exemplified by the widely accepted but unexplained observation that unintentionally-doped FeS_2 single crystals are predominantly *n*-type, whereas thin films are *p*-type. Here we provide a potential resolution to this "doping puzzle", arrived at *via* Hall effect, thermopower, and resistivity measurements on a large set of FeS_2 single crystals and films that span five orders of magnitude in mobility. The results reveal three main findings. First, in addition to crystals, the highest mobility *thin films* in this study are shown to be definitively *n-type*, from both Hall effect and thermopower. Second, as mobility decreases an *apparent* crossover to *p*-type occurs, first in thermopower, then in Hall measurements. This can be understood, however, in terms of the crossover from diffusive to hopping transport that is clearly reflected in resistivity. Third, universal behavior is found for both crystals and films, suggesting a common *n*-dopant, possibly sulfur vacancies. We thus argue that *n*-type doping is facile in FeS_2 films, that apparent *p*-type behavior in low mobility samples can be an artifact of hopping, and that the prevailing notion of predominantly *p*-type films must be revised. These conclusions have deep implications, both for interpretation of prior work on FeS_2 solar cells and for the design of future studies.

*Corresponding authors. Email: leighton@umn.edu, aydil@umn.edu

I. Introduction

Pyrite structure FeS_2 has long been acknowledged as a semiconductor with significant potential as a photovoltaic (PV). A substantial effort to develop pyrite PV began in the mid 1980's, stimulated by pyrite's useful energy gap ($E_g \approx 0.95$ eV) and outstanding visible absorption coefficient ($\alpha > 10^5$ cm^{-1} above 1.2-1.4 eV), which render a 100-nm-thick film capable of absorbing >90 % of the sun's light.[1] Electron mobilities over 300 $cm^2V^{-1}s^{-1}$ and minority carrier diffusion lengths of 100-1000 nm were also demonstrated in pyrite crystals,[1] but the FeS_2 PV effort was nevertheless unsuccessful. Various forms of Schottky and photoelectrochemical solar cells were fabricated from both thin films and bulk crystals, and while the high internal quantum efficiencies and short circuit current densities were promising, open circuit voltages (V_{oc}) remained below 0.2 V, less than 20 % of E_g.[1] Power conversion efficiencies in FeS_2-based solar cells thus never exceeded 3 %,[1] an order of magnitude below the Shockley-Queisser limit. As other thin film PV materials such as CdTe and $Cu(In,Ga)Se_2$ began to show promise in the mid 1990's,[2] interest in pyrite PV waned.

Recently, however, a second wave of interest in FeS_2 for PV applications has emerged.[3-23] This is in large part due to the identification of sulfides, particularly FeS_2, as near-ideal choices for large-scale deployment of solar cells from the perspectives of earth abundance, toxicity, and cost.[3] Sulfur is a waste product, while iron remains one of the cheaper metallic elements to recover from ore. A significant number of researchers are thus applying fresh approaches to the synthesis, characterization, and property measurement of FeS_2-based materials and devices.[3-23]

A notable feature of this second wave of effort with FeS_2 is a focus on fundamental problems, as opposed to the device efforts that have proven unsuccessful.[1-13] Three main issues have emerged:

The origin of the low V_{oc} in pyrite-based solar cells;[1,11,14,17,18,20,24,25] questions regarding phase purity, defects, and stoichiometry;[1,6-12,17,18,20,21,24,25] and the understanding and control of doping.[1,6,7,9-12,17,18,20-22,25] While much remains to be done to address these complex (and often inter-related) issues, significant progress has recently been made, particularly with the first two. Careful studies of *n*-type pyrite single crystals have clearly elucidated surface electronic properties that differ significantly from the bulk, including conductive surface layers,[20] a high density of surface acceptors,[18] and even surface inversion.[20] Such phenomena offer hypotheses for the low V_{oc} in pyrite, which will no doubt be explored. Similar progress has been made with phase purity and stoichiometry. Despite suggestions that secondary phases such as pyrrhotite $Fe_{1-\delta}S$ or marcasite FeS_2 could be deleterious and widespread,[8] several studies have established phase-pure pyrite crystals,[18,20,21] films,[9,12,19,21] and nanostructures,[11,15,17,22] also clarifying stability limits.[21] In terms of stoichiometry, evidence for S vacancies (V_S) as the origin of *n*-type behavior in unintentionally-doped crystals is also accumulating.[18,20]

Progress with the third issue, however (*i.e.*, control and understanding of doping in pyrite), has not been so forthcoming. We note first in this respect that recent high purity, unintentionally-doped pyrite single crystals have been shown to be unambiguously *n*-type,[18,20] with V_S as the suspected dopants,[18,20] consistent with the large majority of the literature. Specifically, unintentionally-doped pyrite crystals are overwhelmingly found from Hall effect measurements to be *n*-type. This is illustrated in Figure 1(a), which plots the magnitude of the room temperature Hall coefficient, R_H, as a function of the carrier mobility, μ, from literature reports on both pyrite films and bulk crystals.[18-20,22,23,26-30] On this plot blue symbols are for electron-like (*i.e.*, apparently *n*-type ($R_H < 0$)) behavior, whereas red symbols are used for hole-like (*i.e.*, apparently *p*-type ($R_H > 0$)) behavior. For bulk crystals, which typically have relatively high μ and thus

populate the top right corner of Figure 1(a), *n*-type majority carriers prevail. The small number of counter-examples often occur in naturally-occurring crystals, where impurities are a concern, or in cases where the Hall effect disagrees with the other premier means to determine the sign of majority carriers, *i.e.*, thermopower, as returned to below.[26,29]

The complexity arises when considering unintentionally-doped *thin films* of FeS_2. The first point here is that the electronic quality of pyrite thin films, as judged from μ, is highly variable. Thin film mobilities up to 200-280 $cm^2V^{-1}s^{-1}$ have been claimed *via* spray pyrolysis[27] and chemical vapor deposition,[31] with an additional handful of other values in the 2 – 80 $cm^2V^{-1}s^{-1}$ range.[5,19,28,29,30] In the great majority of cases, however, pyrite films have μ sufficiently low that they cannot be determined straightforwardly from Hall measurements.[9,12,22,23,28,29,32,33] Some ubiquitous uncontrolled impurity, generating high doping and low μ in pyrite films, is thus often hypothesized, although a high V_S density also seems plausible.[7,22,32-34] This situation explains the modest number of thin film data points in Figure 1(a), exacerbated by the fact that raw data (*i.e.*, Hall coefficient, voltage, or resistance) are often not reported. Notably, and in contrast to bulk crystals, what data are available suggest *p-type* behavior in films. Specifically, as shown in Figure 1(a), while the Hall effect has been reported to indicate either *n*-[29] *or p*-type[19,22,23,27,28,30] majority carriers in FeS_2 films, *p*-type behavior apparently dominates.

Similar conclusions can be reached from thermopower or Seebeck coefficient (*S*) measurements, often employed when the Hall effect is difficult to measure due to low μ.[29] As shown in Figure 1(b), such measurements confirm *n*-type behavior (*i.e.*, $S < 0$, blue points) in bulk single crystals,[26] but appear to support *p*-type conduction (*i.e.*, $S > 0$, red points) in films.[28,29] The number of data points in Figure 1(b) is not impressive, however, due to the large fraction of

cases in the pyrite film literature where "qualitative thermopower" or "hot point probe" measurements are performed.[9,12,23,30,34-37] In those measurements, only the *sign* of *S* is recorded, and thus no data points can be plotted in Figure 1(b). As shown in Table I these "qualitative thermopower" or "hot point probe" measurements (where a carrier type from thermopower is listed but with no value for *S*) are in almost universal support of *p*-type conduction in low mobility FeS_2 thin films. On aggregate, the observations summarized in Figure 1 and Table I have led to the now widely accepted notion[1,7-9,12,18,20,29,30,33] that unintentionally-doped bulk single crystals of pyrite are *n*-type, whereas unintentionally-doped thin films are *p*-type. While some ubiquitous unintentionally-introduced thin film defect or impurity is often cited, the fundamental explanation remains unknown. It is additionally worthwhile to highlight that there are a number of cases, specifically in low μ samples, where R_H and *S* disagree on the sign of the majority carriers,[26,29] as shown in Figure 1(b) and Table I (highlighted in orange), another unresolved issue in pyrite.

Herein we provide a potential resolution to the "doping puzzle" in pyrite FeS_2, *i.e.*, the apparent inversion in sign of the majority carriers from single crystals to films. We do this by comparing 300 K measurements of R_H and *S* on a large set (~100 samples) of unintentionally-doped pyrite single crystals and polycrystalline films, spanning five orders-of-magnitude in apparent μ. Consistent with prior work, the single crystals are found to be unambiguously *n*-type, from both R_H and *S*. In stark contrast to the prevailing view, however, the highest mobility thin films in this study are *also* shown to be unambiguously *n*-type, confirmed by R_H and *S*. As the μ of the thin films decreases an *apparent* transition from electron-like to hole-like majority carriers takes place, first in *S* and then in R_H. While this could be naively interpreted in terms of an $n \rightarrow p$ crossover, we find that the crossover points in R_H and *S* are well correlated with a crossover from

diffusive to hopping transport. This crossover, which is known to be capable of inverting the sign of R_H and S in disordered semiconductors, is tracked in detail *via* temperature-dependent resistivity measurements. We thus conclude that *apparent p*-type behavior in low mobility FeS_2 thin films, whether indicated by R_H or S, can easily be an artifact of hopping. We contend that such films are actually *n*-type, much like higher μ films, challenging the belief that pyrite thin films are predominantly *p*-type and providing a potential resolution to the pyrite "doping puzzle".

II. Experimental Details

II.A Materials synthesis and characterization. Pyrite FeS_2 thin films were synthesized by *ex situ* sulfidation of Fe, as described in greater detail in prior work.[16,21] Briefly, Fe thin films (33 nm thick) were first deposited on chemically-cleaned substrates by either high vacuum DC magnetron sputtering or ultra-high vacuum electron-beam evaporation. Sputtering was done at ~1 Å/s from targets of nominal purity 99.9 or 99.99 %, in 2.3 mTorr of Ar, in a system with a base pressure in the 10^{-8} Torr range. The deposition temperatures were either ambient or 300 °C. Electron beam evaporation was done at 0.5 Å/s from source material of nominal purity 99.99 %, at ambient substrate temperature, in a system with a base pressure in the 10^{-10} Torr range. A wide variety of substrates were explored, including Al_2O_3(0001), soda lime glass, pyrex glass, crystalline quartz (SiO_2), fused quartz (SiO_2), Si(001)/*a*-Si-N, and MgF_2(001). As described earlier,[16,21] sulfidation was achieved in sealed and evacuated (1×10^{-6} Torr) quartz tubes containing 1 mg of 99.999 % pure S, at temperatures of 200 to 600 °C. The majority of the films were sulfidized at 600 °C; some were annealed at temperatures < 400 °C.

Pyrite FeS_2 single crystals were grown *via* the chemical vapor transport (CVT) method, as also described earlier.[21] This employed a sealed and evacuated (1×10^{-6} Torr) quartz vessel in a two-

zone tube furnace, loaded with 2.2 g of FeS_2 powder (99.9 %), 100 mg of $FeBr_2$ (99.999 %) transport agent, and 580 mg of S powder (99.999 %). After an initial 3 day period with an inverted temperature gradient to "clean" the growth zone, hot and cold zone temperatures were set to 670 and 590 °C, respectively, for around 20 days. This resulted in crystals up to 360 mg, with approximately 5 mm (111) facets.

Films and crystals were characterized structurally and chemically *via* wide-angle X-ray diffraction (XRD), Raman spectroscopy, scanning electron microscopy (SEM), energy dispersive spectroscopy (EDS), depth-profiled Auger electron spectroscopy (AES), superconducting quantum interference device (SQUID) magnetometry, and optical absorption spectroscopy. XRD on crystals was performed on a Bruker-AXS D5005 system (powdered crystals) and a Panalytical X-Pert Pro high resolution diffractometer (bulk crystals), using Cu K_α radiation.[16,21] Films were measured using Bruker-AXS PLATFORM and Bruker D8 Discover systems using area detectors, again with Cu K_α. Raman spectroscopy employed a WiTec alpha300R confocal microscope equipped with a UHTS 300 spectrometer and a DV401 CCD detector, SEM and EDS a JEOL field-emission microscope (operated at 15 kV) with a Thermo-Noran Vantage X-ray detector, and AES a Physical Electronics Model 545 with a differentially-pumped Ar sputter source.[16,21] SQUID magnetometry was done at 200 K in a Quantum Design MPMS XL7, and optical absorption was done in a Cary 5000UV-Vis-NIR spectrophotometer in dual beam mode.[16,21] As discussed in more detail below (Section III), a summary of characterization results on films and crystals is provided in Supplemental Material (Figures S1, S2).[40]

II.B Electronic and thermal transport measurements. Temperature-dependent resistivity measurements were made in a Janis cryostat and/or a Quantum Design PPMS, between 2 and

300 K. Indium contacts were employed in a van der Pauw configuration, using both AC (13.7 Hz) and DC excitation depending on the absolute resistance. Extensive checks of contact resistance, current-voltage curves, and AC resistance-current curves were made to ensure Ohmic response and the absence of self-heating. Hall effect measurements were made at 300 K, in applied magnetic fields to ± 90 kOe, using phase-sensitive AC excitation and optimized temperature stability of ± 10 mK. Seebeck coefficient (thermopower) measurements were performed in a vacuum of 10 mTorr in a home-built system at 315 K. FeS_2 samples with coplanar 4-mm-gap electrodes were placed across two thermally isolated Cu blocks, also separated by 4 mm. The temperature of each block was controlled independently (to ± 50 mK) with a dual-channel temperature controller, using thermocouples anchored on each block. As different block temperatures were regulated, the induced thermoelectric voltage was measured *via* Cu leads attached to the blocks. The Seebeck coefficient was then obtained from the slope of thermoelectric voltage *vs*. temperature gradient curves, which extended to 16 K temperature differences. As discussed in more detail below (Section III.A), different substrates were employed (see Supplemental Material Figure S3[40]) to rule out substrate effects as the origin of Seebeck coefficient sign inversion. Any contribution to *S* from the contacts and leads was also investigated, by measuring the thermopower of the electrode metal deposited on a substrate with no pyrite film. The observed *S* was *n*-type and on the order of 0.1-1 μV/K, in contrast to the over 10 times higher *n*- or *p*-type *S* of the polycrystalline FeS_2 films.

III. Results and Analysis

Extensive structural and chemical characterization of our unintentionally-doped pyrite bulk single crystals and polycrystalline thin films has been provided in prior publications.[16,21] In Supplemental Material Figures S1 and S2[40] we provide a brief summary of these characterization

results. In Figure S1, for single crystals, optical imaging, XRD, Raman spectroscopy, and EDS data are shown, confirming the single crystal, single phase, stoichiometric nature of the samples. In Figure S2, for polycrystalline thin films, XRD, Raman spectroscopy, EDS, depth-profiled AES, SQUID magnetometry, optical absorption, and SEM data are shown. These data confirm single-phase, close to stoichiometric, large grain polycrystalline films with the expected optical absorption properties.

III.A Room temperature Hall effect and thermopower measurements. We first focus on 300 K R_H and S measurements performed on bulk single crystals and thin films with a wide range of μ. To this end, Figure 2(a,b) plots R_H and S as a function of the apparent Hall mobility, μ_H, following identical conventions to Figure 1, *i.e.*, blue points for electron-like signs, red points for hole-like signs, and solid triangles and open diamonds for films and crystals, respectively. We explicitly refer to μ_H as an apparent mobility because, as we shall see, some of these μ_H values are sufficiently low that diffusive transport cannot be assumed, and naïve interpretation of R_H is thus hazardous; this will form a key point of our work. The first points to note about Figure 2 are the wide range of μ_H probed (five orders of magnitude) and the substantial reduction in scatter compared to Figure 1. Crystals and films appear to exhibit universal behavior, in fact. Considering first the single crystals, the results are simple, and as expected. These crystals have relatively high μ_H (40-250 $cm^2V^{-1}s^{-1}$) with clearly electron-like R_H and S. Representative raw data to support this are provided in Figure 3(a,b), where the Hall resistivity (ρ_{xy}) is plotted *vs*. applied magnetic field (H) (yielding $R_H = d\rho_{xy}/d\mu_0 H$), and the *negative* thermovoltage ($-\Delta V$) is plotted *vs*. temperature difference (ΔT) (yielding $S = -\Delta V/\Delta T$). ($-\Delta V$ is plotted to facilitate comparison between Hall and thermopower data). For the representative crystal shown, the slope

of both curves is large and negative, indicating *n*-type majority carriers. The Hall response is also linear at all *H* probed, with no evidence of a second carrier type.

The results for polycrystalline thin films are more interesting. As shown in Figure 2, the films studied in this work span a range in μ_H from almost 10 $cm^2V^{-1}s^{-1}$ down to ~10^{-3} $cm^2V^{-1}s^{-1}$. There are two important points to emphasize about this. First, while R_H and *S* are relatively straightforward to measure in high μ_H samples, this is not so at the low μ_H end of this range. In this regime care must be taken to accurately determine very low R_H, including AC detection, a wide *H* range (-90 to + 90 kOe in this case), high *T* stability (± 10 mK at 300 K in this case), and minimization of noise, drift, and contact resistance. Interpretation of low R_H is also challenging, as diffusive transport can no longer be assumed. For thermopower measurements, contributions from the leads, and from substrate effects, must be considered as *S* decreases, as discussed above (Section II.B) and in Supplemental Material Figure S3.[40] Interpretation of low *S* values is also challenging, again due to the possibility of non-diffusive transport. Second, it must be emphasized that complete control over the μ_H of polycrystalline thin films by tuning *ex situ* sulfidation was not achieved in this work. The wide range in μ_H in Figure 2 was rather obtained by synthesizing a large quantity of polycrystalline films, which had variable carrier density, and thus μ_H. As detailed above (Section II.A), the films shown in Figure 2 were in fact synthesized on seven different substrates, using two Fe deposition methods, and variable sulfidation temperatures. While control over carrier density was not obtained, as shown in Supplemental Material Figure S4[40] these films nevertheless exhibit a consistent μ_H-carrier density relation relationship, μ_H scaling as n^{-1}, where *n* is the Hall electron density.

The films exhibit clear and systematic trends in Figure 2, evidencing three distinct regimes. In Regime I, at $\mu_H > 1$ $cm^2V^{-1}s^{-1}$, we find, in stark contrast to claims of predominantly *p*-type conduction in pyrite films, *clear electron-like behavior in both R_H (Figure 2(a)) and S (Figure 2(b))*. Raw data to support this are provided in Figure 3(a,b), where Hall and Seebeck data on a representative film with $\mu_H = 2.2$ $cm^2V^{-1}s^{-1}$ are shown. While R_H and S are smaller than in single crystals, both R_H and S agree on *n*-type transport in these higher μ_H films. ρ_{xy} is again linear in H. In terms of the *origin* of this behavior, note that higher mobility ($\gtrsim 1$ $cm^2V^{-1}s^{-1}$) *n*-type films were obtained on a variety of substrates (Si/Si-N, MgF_2, soda lime glass, quartz, and Al_2O_3), meaning that interdiffusion of some donor impurity is an unlikely explanation. Moreover, as shown in Supplemental Material Figure S5,[40] while Co, Ni, and Cu impurities were detected in these films by Secondary Ion Mass Spectrometry (SIMS), many films have n up to 100 times the concentrations of these elements, implicating an intrinsic rather than extrinsic defect as the dominant *n*-dopant. As in single crystals,[18,20] V_S appears a likely culprit. Regardless of the precise origin, however, what is most important is that the higher μ_H films in this study are definitively *n*-type, in contrast to the prevailing notion.

At lower μ_H Regime II is entered (10^{-2} $cm^2V^{-1}s^{-1} < \mu_H < 1$ $cm^2V^{-1}s^{-1}$), where R_H decreases and maintains an electron-like sign, but both positive and negative signs of S occur (Figure 2(b)), in an apparently chaotic fashion. This is illustrated in Figure 3(c,d) using two representative films, with μ_H of 0.10 and 0.13 $cm^2V^{-1}s^{-1}$. Despite their nearly identical μ_H, the former exhibits electron-like R_H and S, while the latter shows electron-like R_H and hole-like S. As already noted, opposing signs of R_H and S have been sporadically observed before in FeS_2, one proposed explanation relying on two-band transport.[29] Below, we will provide an alternative explanation, acknowledging the significance of low μ. As μ_H decreases further, a final regime of behavior is

found in Figure 2, Regime III, where $\mu_H < 10^{-2}$ $cm^2V^{-1}s^{-1}$. Here, R_H also inverts sign, both R_H and S suggesting hole-like behavior. This is further illustrated in Figure 3(e,f) where raw R_H and S data are shown for a representative film with a low μ_H of 10^{-3} $cm^2V^{-1}s^{-1}$. Again, ρ_{xy} is linear in H. It should be emphasized that the basic structural and chemical characterization data on these films reveal no significant differences over the entire span of μ_H in Figure 2 (see Supplemental Material Figure S6[40]).

III.B Temperature-dependent electronic transport measurements. As already noted, a critical issue for the interpretation of Figure 2 is the low R_H, S, and μ_H found in the lower left region. While R_H and S in higher μ_H samples, in which transport is clearly diffusive, are simple to interpret, this is not so at low μ_H where diffusive band transport can no longer be assumed. In particular, the crossover from diffusive to hopping transport that would be expected in any material as μ decreases (typically below ~1 $cm^2V^{-1}s^{-1}$,[41] notably close to the Regime I / II boundary) is known to suppress R_H and can even invert its sign. Similar complications arise for the interpretation of S. It is thus essential to consider Figure 2 alongside data that elucidate the transport mechanism, making temperature-dependent resistivity (ρ) measurements indispensable.

Figure 4 shows such data, plotting in the top panels (a-c) ρ (log scale) *vs*. T for representative samples in each of the regimes shown in Figure 2. This includes a bulk crystal and a high μ_H (2.2 $cm^2V^{-1}s^{-1}$) film in Regime I (Figure 4(a)), three intermediate μ_H (0.03 – 0.13 $cm^2V^{-1}s^{-1}$) films in Regime II (Figure 4(b)), and a low μ_H (10^{-3} $cm^2V^{-1}s^{-1}$) film in Regime III (Figure 4(c)). Additional insight is provided in Figure 3(d-f) which shows the same data on Zabrodskii plots.[42] These are plots of ln$W$ *vs*. ln$T$, where W, the reduced activation energy, is defined as $W = -d\ln\rho/d\ln T$.[42] This linearizes the $\rho = \rho_0\exp(T_0/T)^m$ form typically expected at low T in

semiconductors, where ρ_0 is the $T \rightarrow \infty$ limit of ρ, T_0 is a characteristic temperature, and m reveals the conduction mechanism. Briefly, $m = 1$ indicates activated, diffusive transport,[43] while $m = ½$ and ¼ indicate Efros-Shklovskii[44] and 3D Mott variable-range hopping (VRH),[45] respectively. VRH is common in doped semiconductors, Mott VRH applying when the density-of-states (DOS) around the Fermi energy (E_F) is approximately constant, Efros-Shklovskii VRH when electron-electron interactions induce a soft-gap in the DOS around E_F.[44,45]

With a mobility of 141 $cm^2V^{-1}s^{-1}$, conduction in the single crystal shown in Figure 4(a,d) would certainly be expected to be diffusive. This is complicated, however, by the anomalous T dependence in Figure 4(a) (note the inflection around 90 K, also evident in Figure 4(d)), which occurs due to the surface conduction documented by Limpinsel *et al*.[20] In essence the insulating FeS_2 interior "freezes out" around this T, the more conductive surface shunting the current at low T. We have made a thorough investigation of this, the results of which will appear elsewhere.[46] Moving on to the relatively high μ_H film in Figure 4(a,d), ρ can be seen to be weakly T-dependent. Considering Figure 4(d), a straight line with negative slope (the black dashed line indicates $m = ½$) is observed at low T (below ~30 K), indicating Efros-Shklovskii VRH. At higher T, however, ln$W$ becomes negative, and increases with T. This indicates conduction close to the insulator-metal transition,[42] certainly not in the hopping regime at 300 K, where the data in Figure 2 were obtained. Both the crystals and films in Regime I are thus clearly in the diffusive transport regime, confirming that R_H and S can be simply interpreted in terms of n-type conduction.

Skipping to Regime III, as illustrated in Figure 4(c,f), the situation is different. In this very low apparent μ_H regime, Figure 4(f) shows adherence to the Efros-Shklovskii form over the entire

range (more than an order of magnitude in T and four orders in ρ), indicating that such films are deep in the VRH regime even at 300 K. Regime III in Figure 2, where both R_H and S have hole-like signs, must thus be interpreted with this in mind, as returned to below. The situation at intermediate μ_H, in Regime II, represents a crossover between Regimes I and III. In this region a spectrum of behaviors is found, evolving non-monotonically with μ_H. Three films are thus shown in Figure 4(b,e), representing three distinct behaviors. The behavior of the film with μ_H = 0.13 $cm^2V^{-1}s^{-1}$ is similar to that seen in Regime III. Efros-Shklovskii VRH is evidenced over the entire T range, indicating that this film is in the hopping regime at 300 K. Vitally, this film (see Figure 3(c,d)) is one in which R_H remains electron-like, while S inverts. On the other hand, the film with μ_H = 0.10 $cm^2V^{-1}s^{-1}$ has behavior similar to Regime I; Efros-Shklovskii VRH occurs at low T, but gives way to diffusive transport by 300 K. In this case (see Figure 3(c,d)), both R_H and S remain electron-like. A final example is provided by the 0.03 $cm^2V^{-1}s^{-1}$ film in Figure 4(b,e), which, despite the slightly lower μ_H, exhibits simple activation at low T (*i.e.*, m = 1) and is clearly not in the Efros-Shklovskii regime at 300 K. This sample also exhibits electron-like R_H.

The apparently complicated behavior in Regime II is thus quite straightforward. While some sample-to-sample variation occurs, films exhibiting diffusive transport at 300 K based on $\rho(T)$ invariably display electron-like R_H and S. When hopping is active at 300 K, however, a sign reversal occurs, first in S. As μ_H decreases further, into Regime III, both R_H *and* S invert, generating the behavior shown in Figures 3(e,f) and 4(c,f). This correlation is reinforced for a large number of films in Supplemental Material Figure S7.[40] The occurrence of hopping conduction is thus essential to understand the signs of R_H and S, a factor not taken into account in prior explanations based on two-band conduction.[29]

IV. Discussion

We now provide a consistent interpretation of Figures 2-4. Beginning with Regime I, specifically with single crystals, the fact that $\mu_H >> 1$ $cm^2V^{-1}s^{-1}$, that the Hall effect is linear, and that $\rho(T)$ provides no evidence of hopping at 300 K, clearly indicate that R_H and S can be simply interpreted. We thus apply $R_H = -1/ne$ (where e is the magnitude of the electronic charge (a positive number)), based on diffusive transport with a dominant majority carrier type. Correspondingly, we interpret S *via* the usual non-degenerate semiconductor approach, $S = -(k_B/e)[(E_C - E_F)/k_BT + a_c]$, where k_B is Boltzmann's constant, E_C is the conduction band onset energy, and a_c is a small constant.[45] Both R_H and S are thus negative, reflecting electrons as majority carriers. This is as expected based on prior work,[18,20,26] the *n*-type doping likely being due to V_S;[18,20] future work to definitively establish this would clearly be worthwhile.

Moving on to the *films* in Regime I, we find $\mu_H \approx$ 1-10 $cm^2V^{-1}s^{-1}$, with $n \sim 10^{19}$ cm^{-3} (Supplemental Material Figure S4[40]). These electron densities are 2-3 orders-of-magnitude higher than in crystals, μ_H being 1-2 orders of magnitude lower. Even in Regime I our films thus have substantially heavier doping and higher disorder than single crystals. S is also reduced, from the 100-200 μVK^{-1} typical of crystals (Table I, Figures 1 and 2) to ~20 μVK^{-1}. The latter is in the range typically seen in pyrite films (10-80 μVK^{-1}, Table I, Figure 1). Critically, however, $\rho(T)$ again provides no evidence of hopping at 300 K, indicating that R_H and S can be interpreted much as for single crystals. Based on Figure 4(a), degenerate semiconductor transport is a possibility, however, meaning that $S = (-\pi^2/3)(k_B^2T/e)(dlnD(E)/dE)_{Ef}$ may be more appropriate, where $D(E)$ is the available DOS.[45] In any event, negative R_H and S indicates electrons as majority carriers, the major issue being the origin of this *n*-doping. Given that numerous films in this study have n greatly in excess of the concentration of metal impurities (Supplemental

Material Figure S5[40]), and that Figure 2 suggests universal behavior (*i.e.*, a single R_H-n or μ_H –n relationship) for both films and crystals, V_S is again a strong possibility. The V_S density may be difficult to control in FeS_2 films, certainly when synthesized by the methods employed here.

In Regime II, $\mu_H < 1$ $cm^2V^{-1}s^{-1}$ is encountered for the first time, hopping transport becoming a possibility. Although not widely discussed in the pyrite literature, the influence of hopping on R_H and S has a long history. Consider first the Hall effect in hopping transport, which was studied in the context of amorphous (a) Si and Ge in the 1970's. A first surprise was provided by Friedman[47] in 1971 who showed that even when conduction proceeds by extended states, when these are near the mobility edge, E_μ, R_H can be suppressed by an order of magnitude and, most significantly, R_H is always electron-like, even in *p*-type materials. Experiments by Le Comber *et al*.[48] further revealed a *double* sign reversal, where a-Si films in the hopping regime doped *n*-type (with P) had $R_H > 0$, while films doped *p*-type (with B) had $R_H < 0$. Numerous theoretical works have been devoted to this topic, but it is fraught with complications. The three-site "triads" of Gal'perin *et al*. are understood to be the elementary sources of the hopping Hall voltage,[49] but both the magnitude and sign of R_H are difficult to calculate, although the double sign reversal can be qualitatively reproduced.[49,50] The relevance to low μ_H pyrite films was pointed out in our earlier work,[16] where an apparent sign reversal in R_H on entry into a regime of a specific type of intergranular hopping, due to nanoscale unreacted Fe clusters, was discovered. In the current work this is seen to be more generally important.

Thermopower in the hopping regime is similarly rich. An important fact, which has again not been widely discussed in the pyrite literature, is that hopping impacts both the magnitude and sign of *S*. In VRH this is because carriers with both positive and negative energies with respect to

E_F contribute to thermopower.[51-53] S thus vanishes for a DOS symmetric around E_F, DOS asymmetry being the essential factor, making sign reversal easily possible. This was handled by Zvyagin and Overhof in the 70's by writing:[51,52]

$$S = -\frac{k_B}{e}\int_{-W}^{W}\frac{E}{k_BT}N(E)dE\Big/\int_{-W}^{W}N(E)dE \qquad (1)$$

where E is the energy with respect to E_F, and W is the energy interval around which hopping proceeds at temperature T. For a locally linear $D(E)$ this yields

$$S = -\frac{k_B^2}{3e}C^2(T_0T)^{\frac{1}{2}}\left(\frac{dlnD(E)}{dE}\right)_{E_F} \qquad (2),$$

where C is a constant. The sign of S is thus dictated by $d\ln D(E)/dE$ at E_F, a situation thought to play an important role in the double sign reversal of R_H and S in *a*-Si and Ge.[48-53]

The discussion above directly informs the interpretation of Regime II in Figures 2-4. First, the sign reversal of the 300 K S in films exhibiting hopping at 300 K is not at all unexpected, without precedent, or without theoretical basis. The same can be said of the scatter in S in Regime II (Figure 2(a)), as the magnitude and sign of S become highly sensitive to the details of $D(E)$ near E_F. This is illustrated in the schematic DOS of a disordered semiconductor shown in Figure 5, where a donor band overlaps the conduction band. Here, E_F located at E_1, deep in the conduction band, would result in diffusive transport, R_H and S being easily interpreted. E_F in or around the donor band, however, is expected for hopping transport. As an illustration, we note that placing E_F at positions E_2, E_3, E_4, or E_5 would result, based on equation (2), in positive, negligible, negative, and negligible S, respectively. Similar uncertainty in the sign of S persists in the Efros-Shklovskii VRH regime of interest in light of Figure 4. As shown in the inset to Figure 5, and

also discussed in prior work, the sign of S in that case, where $D(E)$ is coulomb-gapped, again arises only from DOS asymmetry (see equation (1)), and is thus variable.[51-53]

In light of the above, the surprising feature in the data of Figure 2 is not that S can reverse sign, but rather that R_H remains apparently unaffected by hopping in Regime II, only inverting deep into the hopping regime at ~0.01 $cm^2V^{-1}s^{-1}$. One important observation here is that R_H is a transport quantity, whereas thermopower is a thermodynamic one, measured under *open circuit conditions*. There are numerous scenarios where thermodynamic averages and transport results can be substantially different, and future theoretical work in this area specific to pyrite films would clearly be worthwhile. Two-band/channel conduction analysis explicitly including hopping could also be a fruitful avenue. In any case, the most important conclusion from Figures 2-4 is that, unlike the approach taken in much of the pyrite literature, S is clearly not a reliable indicator of the majority carrier type in low μ pyrite films where R_H is difficult to measure. Quite the opposite is evidenced in Regime II of Figure 2. In Regime III, where hopping transport dominates, eventually both R_H and S become inverted and small, the magnitudes reaching ~10^{-3} cm^3C^{-1} and ~ 10 μVK^{-1}. Based on the above, these small positive values, deep in the Efros-Shklovskii VRH regime, should clearly not be interpreted as *p*-type conduction.

Although it does not impact the general arguments made here, one additional important point is the exact nature of the hopping conduction observed in Regimes II and III. As briefly alluded to above, and discussed in detail in our prior work,[16,21] the $\rho = \rho_0 \exp(T_0/T)^{1/2}$ form is consistent not only with conventional Efros-Shklovskii VRH in a homogeneous doped semiconductor, but also intergranular hopping between nanoscopic conductive clusters in an insulating matrix. The latter mechanism was deduced in our earlier work on FeS_2 films in two distinct contexts,[16,21]

highlighting the issue of local conductance variations in pyrite arising due to compositional fluctuations. A fuller discussion of the relation between the conventional Efros-Shklovskii mechanism and intergranular transport in pyrite was provided in Ref. 21. We note here simply that: (a) Regardless of the exact nature of the hopping conduction the general arguments above regarding the sign inversion and magnitude of R_H and S remain valid; and (b) Intergranular-type hopping may well play a role in at least some instances in the current work, potentially causing the quite large T_0 values and thus the existence of hopping transport up to 300 K.

While the above interpretation of the origin of the doping puzzle substantially elucidates a number of issues in unintentionally-doped FeS_2 films, we note that some outstanding questions nevertheless remain. First, it should be recalled that there are a handful of *p*-type thin film pyrite publications that have reported μ in the 2-80 $cm^2V^{-1}s^{-1}$ range,[5,19,28,30] one at 200 $cm^2V^{-1}s^{-1}$ (see Figure 1 and Table I).[27] Raw Hall data are often not provided in these cases, however (or are not measured to large H), making it difficult to assess the evidence for positive R_H. ρ(T) data are also often not provided, making it difficult to assess the conduction mechanism. Nevertheless, hopping transport does not appear capable of explaining *p*-type behavior in cases with such high μ. Further work to reproduce and verify these conclusions, and elucidate the possibility of a true *p*-type dopant, is imperative. Second, given the recent work that has demonstrated surface conduction, and even surface inversion in *n*-type FeS_2 crystals,[20] it is important to consider surface conduction as a possible origin of the behavior seen here. None of the key indicators of surface conduction are present in the films studied here, however. Prior work on bulk *n*-type crystals has demonstrated certain features in the temperature and thickness dependence of transport to be particularly useful for detecting surface conduction,[20,46] but no such features arise in our films. Moreover, consistent with our own bulk single crystal data,[46] and the arguments of

Limpinsel *et al*.[20] and Caban-Acevedo *et al*.,[18] surface inversion is increasingly unlikely as *n*-doping becomes heavier, and surface band-bending is restricted. The apparent *n* values in the films in this work range from 5×10^{18} to $\sim10^{21}$ cm^{-3}, much higher than in single crystals, rendering surface inversion an unlikely explanation for the apparent inversion in R_H and *S* in Figure 2. This remains true even for *grain surface conduction*, another issue that must be considered here.

V. Summary

In conclusion, we have presented a comprehensive data set that encompasses Hall effect, thermopower, and resistivity measurements on a large set of bulk single crystal and polycrystalline pyrite FeS_2 films, aiming to clarify the puzzling observation that unintentionally-doped crystals are predominantly *n*-type, whereas thin films are apparently *p*-type. The results not only indicate unambiguously *n*-type behavior in higher mobility films, but also show that the apparent *p*-type behavior in lower mobility films can easily arise as an artifact of hopping conduction. This challenges the widespread belief in predominant *p*-type conduction in pyrite films, underscoring the need to combine Hall effect and thermopower measurements of majority carrier type with temperature-dependent transport measurements to establish conduction mechanisms. These results are important both for interpretation of prior work, and for the design of future pyrite photovoltaic devices.

Acknowledgments

This work was supported by the NSF under DMR-1309642, in part by NSF MRSEC under DMR-1420013, and by the customers of Xcel energy through a grant from the Renewable Development Fund. Parts of this work were carried out in the Characterization Facility, UMN,

which receives partial support from the NSF MRSEC program. Use of the SARISA SIMS instrument (MSD, ANL) was supported by the U.S. Department of Energy, Office of Science, Materials Sciences and Engineering Division. We thank B. Shklovskii and K. Reich for numerous fruitful discussions and Dr. Alex Zinovev for assistance with SIMS data acquisition.

References

1. Ennaoui, A. *et al.* Iron disulfide for solar energy conversion. *Sol. Energy Mater. Sol. Cells* **29,** 289–370 (1993).

2. Wolden, C. A. *et al.* Photovoltaic manufacturing: Present status, future prospects, and research needs. *J. Vac. Sci. Technol. A* **29,** 030801 (2011).

3. Wadia, C., Alivisatos, A. P. & Kammen, D. M. Materials availability expands the opportunity for large-scale photovoltaics deployment. *Environ. Sci. Technol.* **43,** 2072–2077 (2009).

4. Puthussery, J., Seefeld, S., Berry, N., Gibbs, M. & Law, M. Colloidal iron pyrite (FeS_2) nanocrystal inks for thin-film photovoltaics. *J. Am. Chem. Soc.* **133,** 716–719 (2011).

5. Bi, Y., Yuan, Y., Exstrom, C. L., Darveau, S. A. & Huang, J. Air stable, photosensitive, phase pure iron pyrite nanocrystal thin films for photovoltaic application. *Nano Lett.* **11,** 4953–4957 (2011).

6. Sun, R., Chan, M. K. Y. & Ceder, G. First-principles electronic structure and relative stability of pyrite and marcasite: Implications for photovoltaic performance. *Phys. Rev. B* **83,** 235311 (2011).

7. Sun, R., Chan, M. K. Y., Kang, S. Y. & Ceder, G. Intrinsic stoichiometry and oxygen-induced p-type conductivity of pyrite FeS_2. *Phys. Rev. B* **84,** 035212 (2011).

8. Yu, L. *et al.* Iron chalcogenide photovoltaic absorbers. *Adv. Energy Mater.* **1,** 748–753 (2011).

9. Berry, N. *et al.* Atmospheric-pressure chemical vapor deposition of iron pyrite thin films. *Adv. Energy Mater.* **2,** 1124–1135 (2012).

10. Hu, J., Zhang, Y., Law, M. & Wu, R. First-principles studies of the electronic properties of native and substitutional anionic defects in bulk iron pyrite. *Phys. Rev. B* **85,** 85203 (2012).

11. Cabán-Acevedo, M., Faber, M. S., Tan, Y., Hamers, R. J. & Jin, S. Synthesis and properties of semiconducting iron pyrite (FeS_2) nanowires. *Nano Lett.* **12,** 1977–1982 (2012).

12. Seefeld, S. *et al.* Iron pyrite thin films synthesized from an $Fe(acac)_3$ ink. *J. Am. Chem. Soc.* **135,** 4412–4424 (2013).

13. Steinhagen, C., Harvey, T. B., Stolle, C. J., Harris, J. & Korgel, B. A. Pyrite nanocrystal solar cells: Promising, or fool's gold? *J. Phys. Chem. Lett.* **3,** 2352–2356 (2012).

14. Lazic, P. *et al.* Low intensity conduction states in FeS_2: implications for absorption, open-circuit voltage and surface recombination. *J. Phys. Condens. Matter* **25,** 465801 (2013).

15. Lucas, J. M. *et al.* Ligand-controlled colloidal synthesis and electronic structure characterization of cubic iron pyrite (FeS_2) nanocrystals. *Chem. Mater.* **25,** 1615–1620 (2013).

16. Zhang, X. *et al.* Crossover from nanoscopic intergranular hopping to conventional charge transport in pyrite thin films. *ACS Nano* **7,** 2781–2789 (2013).

17. Cabán-Acevedo, M. *et al.* Synthesis, characterization, and variable range hopping transport of pyrite (FeS_2) nanorods, nanobelts, and nanoplates. *ACS Nano* **7,** 1731–1739 (2013).

18. Cabán-Acevedo, M. *et al.* Ionization of high-density deep donor defect states explains the low photovoltage of iron pyrite single crystals. *J. Am. Chem. Soc.* **136,** 17163–17179 (2014).

19. Shukla, S. *et al.* Iron pyrite thin films counter electrodes for dye-sensitized solar cells: high efficiency for iodine and cobalt redox electrolyte cells. *ACS Nano* **8,** 10597–10605 (2014).

20. Limpinsel, M. *et al.* An inversion layer at the surface of n-type iron pyrite. *Energy Environ. Sci.* **7**, 1974–1989 (2014).

21. Zhang, X. *et al.* Phase stability and stoichiometry in thin film iron pyrite: Impact on electronic transport properties. *ACS Appl. Mater. Interfaces* **7,** 14130–14139 (2015).

22. Shukla, S. *et al.* Origin of photocarrier losses in iron pyrite (FeS_2) nanocubes. *ACS Nano* **10,** 4431–4440 (2016).

23. Kinner, T. *et al.* Majority carrier type control of cobalt iron sulfide ($Co_xFe_{1-x}S_2$) pyrite nanocrystals. *J. Phys. Chem. C* **120,** 5706–5713 (2016).

24. Birkholz, M., Fiechter, S., Hartmann, A. & Tributsch, H. Sulfur deficiency in iron pyrite (FeS_{2-x}) and its consequences for band-structure models. *Phys. Rev. B* **43,** 11926–11936 (1991).

25. Büker, K., Alonso-Vante, N. & Tributsch, H. Photovoltaic output limitation of n-FeS_2 (pyrite) Schottky barriers: A temperature-dependent characterization. *J. Appl. Phys.* **72,** 5721–5728 (1992).

26. Willeke, G., Blenk, O., Kloc, C. & Bucher, E. Preparation and electrical transport properties of pyrite (FeS_2) single crystals. *J. Alloys Compd.* **178,** 181–191 (1992).

27. Yamamoto, A. *et al.* Pyrite (FeS_2) thin films prepared by spray method using $FeSO_4$ and $(NH_4)_2S_x$. *Sol. Energy Mater. Sol. Cells* **75,** 451–456 (2003).

28. Lichtenberger, D., Ellmer, K., Schieck, R., Fiechter, S. & Tributsch, H. Structural, optical, and electrical properties of polycrystalline iron pyrite layers deposited by reactive d.c. magnetron sputtering. *Thin Solid Films* **246,** 6–12 (1994).

29. Ares, J. R., Ferrer, I. J. & Sánchez, C. R. Majority carriers in pyrite thin films: An analysis based on Seebeck and Hall coefficient measurements. *Thin Solid Films* **431–432,** 511–513 (2003).

30. Willeke, G., Dasbach, R., Sailer, B. & Bucher, E. Thin pyrite (FeS_2) films prepared by magnetron sputtering. *Thin Solid Films* **213,** 271–276 (1992).

31. Note that in the following citation the reported values of resistivity, carrier density, and mobility do not appear to be self-consistent. With the stated values of the resistivity and carrier density, a mobility of only 11 $cm^2V^{-1}s^{-1}$ is obtained; the origin of the discrepancy with the 280 $cm^2V^{-1}s^{-1}$ quoted in this paper is unknown. Takahashi, N., Nakatani, Y., Yatomi, T. & Nakamura,

T. Growth of single-crystal pyrite films by atmospheric pressure chemical vapor deposition. *Chem. Mater*. **15**, 1763-1765 (2003).

32. Oertel, J., Ellmer, K., Bohne, W., Rohrich, J. & Tributsch, H. Growth of n-type polycrystalline pyrite (FeS_2) films by metalorganic chemical vapour deposition and their electrical characterization. *J. Cryst. Growth* **198/199,** 1205–1210 (1999).

33. Ares, J. R. *et al.* Evolution of the Seebeck coefficient during the formation and crystallization of pyrite thin films. *J. Phys. Condens. Matter* **10,** 4281–4289 (1998).

34. Smestad, G. *et al.* Photoactive thin film semiconducting iron pyrite prepared by sulfurization of iron oxides. *Sol. Energy Mater.* **20,** 149–165 (1990).

35. Bausch, S. *et al.* Preparation of pyrite films by plasma-assisted sulfurization of thin iron films. *Appl. Phys. Lett.* **57,** 25–27 (1990).

36. Soukup, R. J., Prabukanthan, P., Ianno, N. J., Sarkar, A., Kamler, C. A. & Sekora D. G. Formation of pyrite (FeS_2) thin films by thermal sulfurization of dc magnetron sputtered iron. *J. Vac. Sci. Technol. A* **29,** 011001 (2011).

37. Chatzitheodorou, G. *et al.* Thin photoactive FeS_2 (pyrite) films. *Mater. Res. Bull.* **21,** 1481–1487 (1986).

38. Ares, J. R., Ferrer, I. J., Cuevas, F. & Sánchez, C. R. Growth of pyrite thin-films investigated by thermoelectric measurements. *Thin Solid Films* **387,** 97-99 (2001).

39. Thomas, B. *et al.* Formation of secondary iron-sulphur phases during the growth of polycrystalline iron pyrite (FeS_2) thin films by MOCVD. *J. Mater. Sci. Electron.* **9,** 61-64 (1998).

40. See Supplemental Material at [*URL*] for additional information on structural/chemical characterization of single crystals and thin films; experimental details for thermopower measurements; electrical, impurity analysis, and characterization data on thin films; and correlations between hopping conduction and the Hall/Seebeck coefficient.

41. Stafstrom, S. Electron localization and the transition from adiabatic to nonadiabatic charge transport in organic conductors. *Chem. Soc. Rev*. **39**, 2484-2499 (2010).

42. Zabrodskii, A. G. The Coulomb gap: the view of an experimenter. *Phil. Mag. B.* **81** 1131-1151 (2001).

43. We note that nearest neighbor hopping also results in $m = 1$, albeit with different activation energy and doping dependence than a simple activation process.

44. Shklovskii, B. I. & Efros, A. L. *Electronic Properties of Doped Semiconductors* (Springer-Verlag, 1984).

45. Mott, N. F. *Metal Insulator Transitions*. 2nd ed. (Taylor and Francis, 1990).

46. Walter, J., Zhang, X., Mork, F., Hool, R., Manno, M., Aydil, E. & Leighton, C., unpublished (2017).

47. Friedman, L. Hall conductivity of amorphous semiconductors in the random phase model. *J. Non-Cryst. Solids* **6**, 329-341 (1971).

48. Le Comber, P. G., Jones, D. I. & Spear, W. E. Hall effect and impurity conduction in substitutionally doped amorphous silicon. *Phil. Mag*. **35**, 1173-1187 (1977).

49. Gal'perin, Yu. M., German, E. P. & Karpov, V. G. Hall effect under hopping conduction conditions. *Sov. Phys. JETP* **72**, 193-200 (1991).

50. Kakalios, J. Physical interpretation of the Hall effect in amorphous semiconductors. *J. Non-Cryst. Solids* **114**, 372-374 (1989).

51. Zvyagin, I. P. On the theory of hopping transport in disordered semiconductors. *Phys. Stat. Sol.* **58**, 443-449 (1973); Zvyagin, I. P. The hopping thermopower, in *Hopping Transport in Solids* eds. Pollak, M. & Shklovskii, B (Elsevier, 1991).

52. Overhof, H. Thermopower calculation for variable range hopping – application to a-Si. *Phys. Stat. Sol.* **67**, 709-714 (1975).

53. Lewis, A. J. Conductivity and thermoelectric power of amorphous germanium and amorphous silicon. *Phys. Rev. B.* **13**, 2565-2575 (1976).

Tables and Captions

FeS_2	Synthesis method	ρ(300K) [Ωcm]	S(300 K) [μVK^{-1}]	Thermopower	Hall effect	μ_H(300K) [$cm^2V^{-1}s^{-1}$]	Reference
Thin film	Sulfidation of Fe	Not measured	0-80	h^+-like	Beneath detection	Beneath detection	Ares *et al.* [33]
Thin film	Sulfidation of Fe	0.1	70	h^+-like	e^--like	6.7	Ares *et al.* [29]
Thin film	Sulfidation of Fe	Not measured	70-80	h^+-like	Not measured	Not measured	Ares *et al.* [38]
Thin film	Sulfidation of Fe	0.50-0.58	Not measured	h^+-like	Not measured	Not measured	Soukup *et al.* [36]
Thin film	Plasma-assisted sulfidation of Fe	1	Not measured	h^+-like	Not measured	Not measured	Bausch *et al.* [35]
Thin film	Sulfidation of Fe_2O_3/Fe_3O_4	Not measured	Not measured	h^+-like	Not measured	Not measured	Smestad *et al.* [34]
Thin film	Annealing of $Fe(acac)_3$ ink	1.35	Not measured	h^+-like	Beneath detection	Beneath detection	Seefeld *et al.* [12]
Thin film	Pyrite nanocrystal coating/hydrazine tr.	5.9/1.7	Not measured	h^+-like	h^+-like	0.3/0.2	Kinner *et al*. [23]
Thin film	Pyrite nanocrystal coating	Not reported	Not measured	Not measured	h^+-like	80	Bi *et al.* [5]
Thin film	Pyrite nanocrystal coating	11.2	Not measured	Not measured	h^+-like	0.1	Shukla et al. [22]
Thin film	Spray pyrolysis	0.59	Not measured	Not measured	h^+-like	2.12	Shukla *et al*. [19]
Thin film	Spray pyrolysis	0.425	Not measured	Not measured	h^+-like	210	Yamamoto *et al.* [27]
Thin film	Reactive sputtering (Fe target)	0.3	90	h^+-like	Beneath detection	Beneath detection	Lichtenberger *et al.* [28]
Thin film	Reactive sputtering (Fe target)	0.003	10	h^+-like	h^+-like	25	Lichtenberger *et al.* [28]
Thin film	Reactive sputtering (FeS_2 target)	0.25	Not measured	h^+-like	h^+-like	5	Willeke *et al.* [30]
Thin film	CVD	1	50	h^+-like	Not measured	Not measured	Thomas *et al.* [39]
Thin film	CVD	0.97	Not measured	Not measured	Not reported	280	Takahashi *et al.* [31]
Thin film	CVD	1.5 ± 0.5	Not measured	h^+-like	Beneath detection	Beneath detection	Berry *et al.* [9]
Thin film	CVD	0.4	55	h^+-like	Beneath detection	Beneath detection	Oertel *et al.* [32]
Thin film	CVD	0.001-1	Not measured	h^+-like	Not measured	Not measured	Chatzitheodorou *et al.* [37]
Syn. crystal	CVT	142	11	e^--like	h^+-like	5.3	Willeke *et al.* [26]
Syn. crystal	CVT	2.1	320	e^--like	e^--like	172	Willeke *et al.* [26]
Syn. crystal	CVT	2.8	230	e^--like	e^--like	113	Willeke *et al*.[26]
Syn. crystal	Flux	5.1	Not measured	Not measured	e^--like	245	Limpinsel *et al*. [20]
Syn. crystal	CVT	114	Not measured	Not measured	e^--like	50	Cabán-Acevedo *et al*. [18]

Table I: Literature review of carrier types in unintentionally-doped FeS_2 from Hall effect and thermopower. The 300 K resistivity (ρ), 300 K Seebeck coefficient (S), carrier type from thermopower and Hall effect, and 300 K apparent Hall mobility (μ_H) are shown for both films (yellow) and synthetic crystals (green).[5,9,12,18,19,20,22,23,26-39] The synthesis method and relevant citation are shown; CVD is chemical vapor deposition and CVT is chemical vapor transport. When a thermopower carrier type is listed, but with no corresponding S, this resulted from "qualitative thermopower", or "hot point probe" measurements, where only the sign of S is determined. The cases where carrier types are available from both thermopower (quantitative or qualitative) *and* Hall, are highlighted in color; purple indicates consistency between the two, orange inconsistency.

Figure Captions

Figure 1. Summary of the literature on carrier type in unintentionally-doped pyrite FeS_2 from Hall effect and thermopower. The room-temperature (~300 K) Hall coefficient (R_H) (a)[18,19,20,22,23,26-30] and Seebeck coefficient (S) (b)[26,28,29] are plotted *vs*. the reported Hall carrier mobility (μ) for FeS_2 in various forms. The red/blue symbols indicate the apparent majority carrier type (hole/electron-like) based on the sign of R_H and S. Explicitly, "hole-like" is associated with $R_H > 0$, $S > 0$, while "electron-like" is associated with $R_H < 0$, $S < 0$. Data are distinguished for thin films, synthetic single crystals and natural single crystals.

Figure 2. Hall effect, thermopower, and apparent carrier types in the unintentionally-doped FeS_2 films and crystals from this study. The room-temperature (~300 K) Hall coefficient (R_H) (a) and Seebeck coefficient (S) (b) are plotted *vs*. the apparent Hall carrier mobility (μ_H) for the polycrystalline films and synthetic single crystals in the current study. Again, the red/blue symbols indicate the apparent carrier type (hole/electron-like) based on the sign of R_H and S. Explicitly, "hole-like" is associated with $R_H > 0$, $S > 0$, while "electron-like" is associated with $R_H < 0$, $S < 0$. The arrows in panel (a) indicate upper bounds on μ_H and R_H,, *i.e.* points at the limit of detection. The vertical dashed lines and markings "I", "II" and "III" indicate the three regimes discussed in the text.

Figure 3. Representative raw data from Hall effect and thermopower measurements. The left panels show the magnetic field (H) dependence of the zero-field-background-subtracted Hall resistivity (ρ_{xy}) in regimes I (a), II (c) and III (e). The right panels show the temperature gradient (ΔT) dependence of the *negative* thermoelectric voltage ($-\Delta V$) in regimes I (b), II (d) and III (f).

Note that $-\Delta V$ is plotted, to facilitate comparison to the Hall data. Dashed lines in all cases are straight line fits. Two samples are plotted in Region I (one crystal, one film), and two films are plotted in Region II (one where R_H and S agree on the sign of the majority carriers, one where they do not). In all cases the samples are labeled with their room temperature μ_H. All data are at room temperature (~300 K).

Figure 4. Temperature-dependent electronic transport measurements. In the top panel the temperature (T) dependence of the resistivity (ρ) is shown in (a) Regime I, (b) Regime II, and (c) Regime III. The bottom panel shows ln W *vs.* ln T generated from the data in the top panel, where $W = -d\ln\rho/d\ln T$. Slopes of $m = ½$ and 1 are shown, where m is the exponent in $\rho = \rho_0 \exp(T_0/T)^m$. The room temperature (~300 K) apparent Hall mobility (μ_H) for each sample is labelled. Two samples are shown in Regime I (one crystal, one film), and three films are plotted in Regime II, illustrating the behaviors discussed in the text.

Figure 5. Schematic density-of-states. Schematic available density-of-states ($D(E)$) *vs*. energy (E) plot for the illustrative case of a Gaussian donor band (DB, blue) overlapping with a free-electron-like conduction band (CB, green). Five illustrative potential Fermi energy locations, E_1 through E_5, are indicated by the red dashed lines. The inset shows a density-of-states with a Coulomb gap of width Δ_C around a potential Fermi energy location E_6.

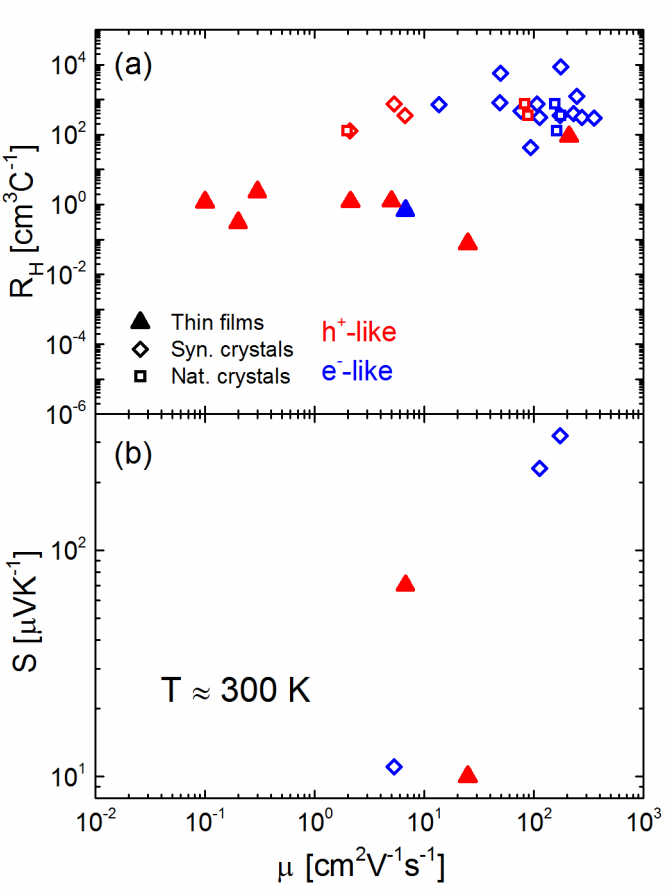
(a)
(b)
Thin films
Syn. crystals
Nat. crystals
h+-like
e--like
T ≈ 300 K
RH [cm3C-1]
S [μVK-1]
μ [cm2V-1s-1]

Figure 1

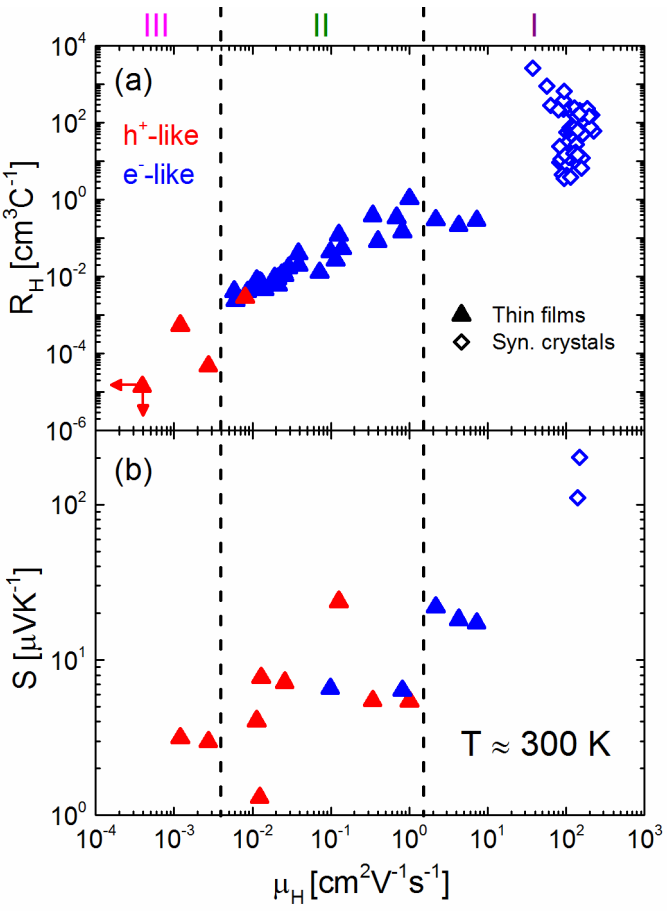
III
II
I
(a)
h+-like
e--like
Thin films
Syn. crystals
RH [cm3C-1]
(b)
T ≈ 300 K
S [μVK-1]
μH [cm2V-1s-1]

Figure 2

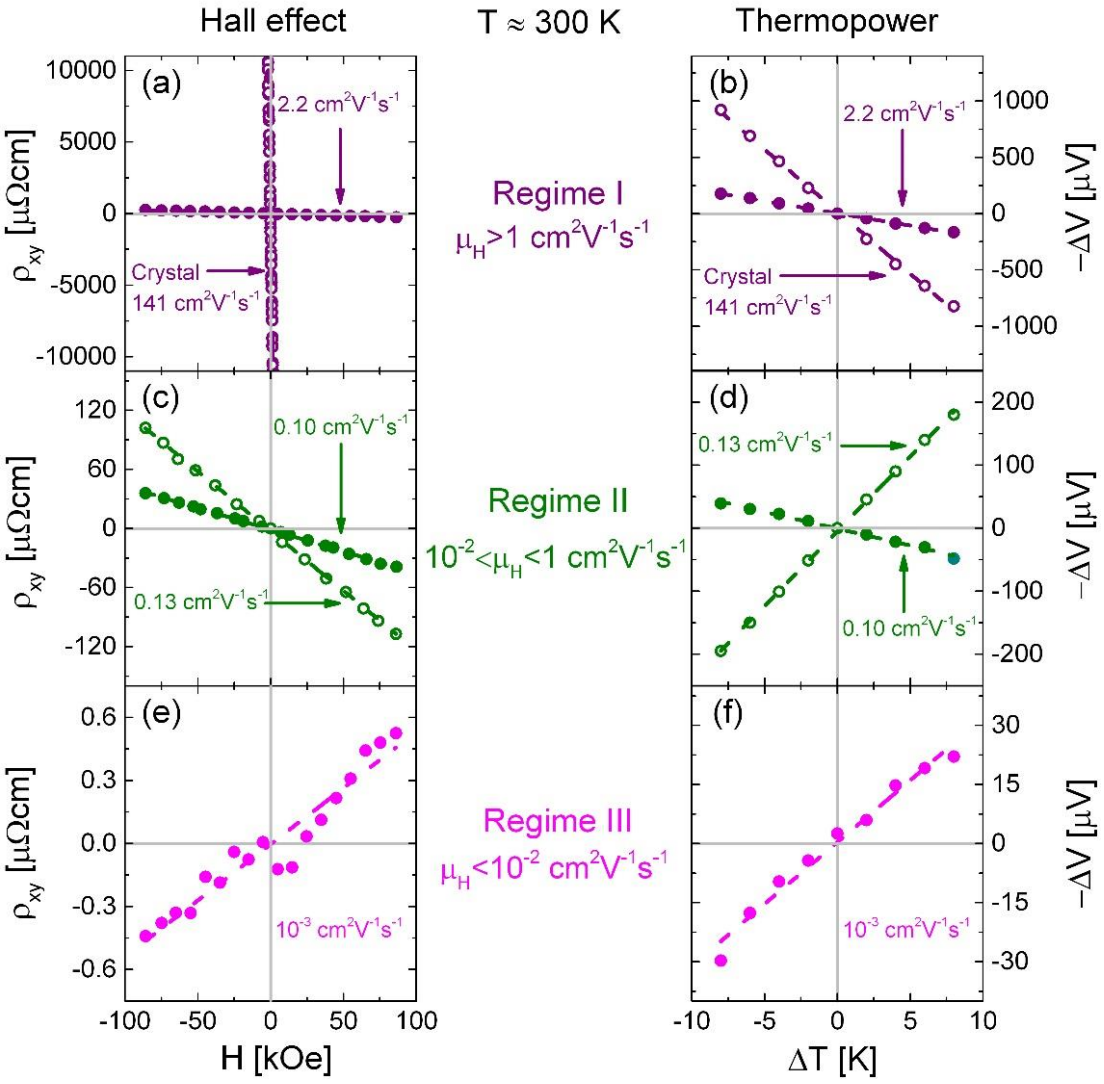
Hall effect
T ≈ 300 K
Thermopower
(a)
(b)
(c)
(d)
(e)
(f)
2.2 cm²V⁻¹s⁻¹
Crystal
141 cm²V⁻¹s⁻¹
0.10 cm²V⁻¹s⁻¹
0.13 cm²V⁻¹s⁻¹
10⁻³ cm²V⁻¹s⁻¹
Regime I
μH>1 cm²V⁻¹s⁻¹
Regime II
10⁻²<μH<1 cm²V⁻¹s⁻¹
Regime III
μH<10⁻² cm²V⁻¹s⁻¹
ρxy [μΩcm]
−ΔV [μV]
H [kOe]
ΔT [K]

Figure 3

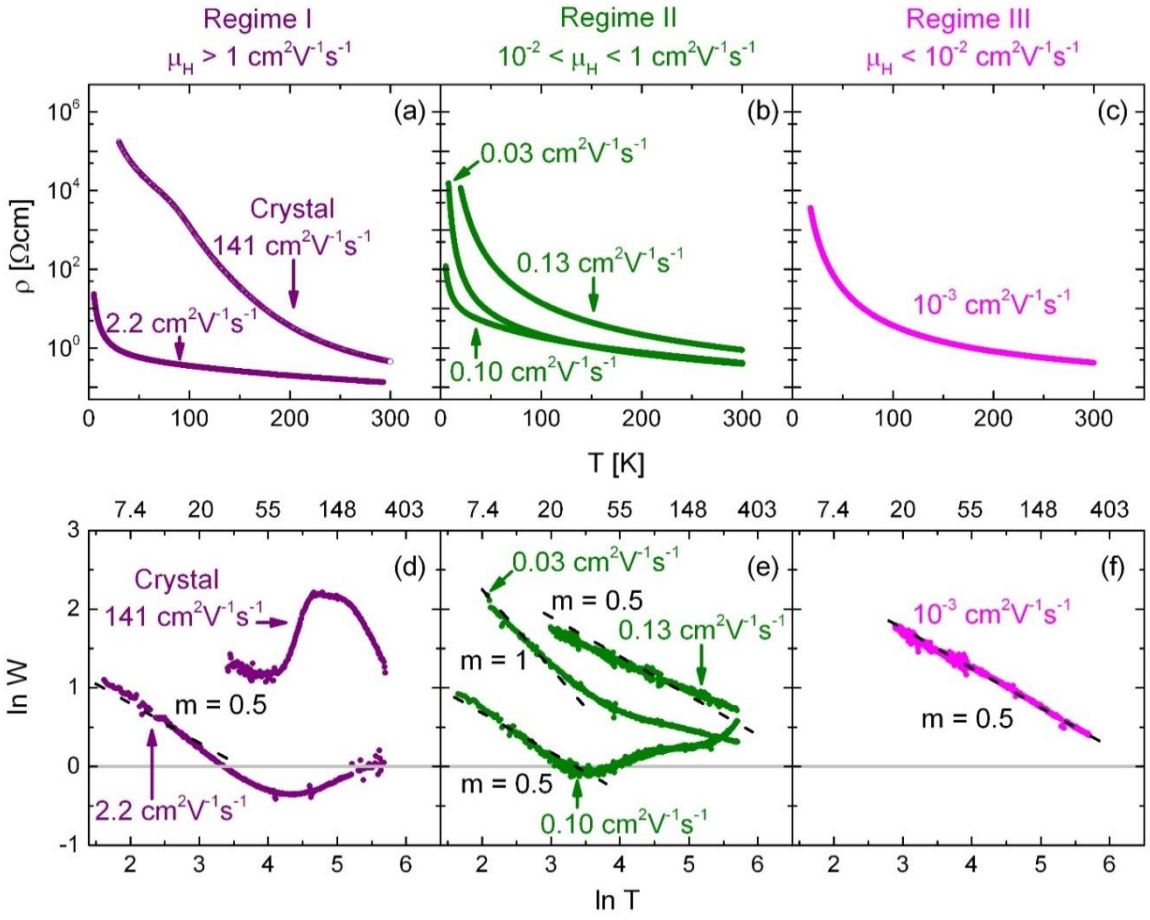
Regime I
μH > 1 cm2V-1s-1
Regime II
10-2 < μH < 1 cm2V-1s-1
Regime III
μH < 10-2 cm2V-1s-1
(a)
(b)
(c)
ρ [Ωcm]
Crystal
141 cm2V-1s-1
2.2 cm2V-1s-1
0.03 cm2V-1s-1
0.13 cm2V-1s-1
0.10 cm2V-1s-1
10-3 cm2V-1s-1
T [K]
(d)
(e)
(f)
ln W
m = 0.5
m = 1
ln T

Figure 4

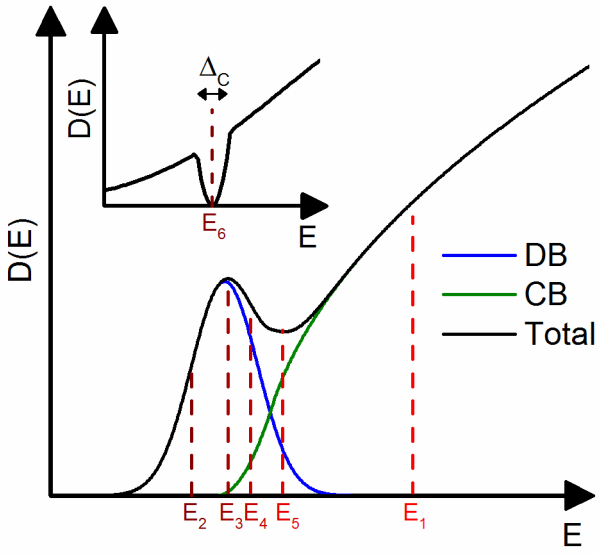

Figure 5